energies

MDPI

Article

Energy Simulation of a Holographic PVT Concentrating System for Building Integration Applications

Julia Marín-Sáez [1], Daniel Chemisana [1,*], Álex Moreno [1], Alberto Riverola [1], Jesús Atencia [2] and María-Victoria Collados [2]

[1] Applied Physics Section of the Environmental Science Department, Polytechnic School, University of Lleida, Lleida 25001, Spain; jmarin@macs.udl.cat (J.M.-S.); alex.moreno@udl.cat (Á.M.); alberto.riverola@macs.udl.cat (A.R.)

[2] Applied Physics Department, Aragon Institute of Engineering Research (I3A), University of Zaragoza, Zaragoza 50009, Spain; atencia@unizar.es (J.A.); vcollado@unizar.es (M.-V.C.)

* Correspondence: daniel.chemisana@macs.udl.cat; Tel.: +34-973-003-711

Academic Editors: Francesco Calise and Massimo Dentice d'Accadia
Received: 1 June 2016; Accepted: 12 July 2016; Published: 25 July 2016

Abstract: A building integrated holographic concentrating photovoltaic-thermal system has been optically and energetically simulated. The system has been designed to be superimposed into a solar shading louvre; in this way the concentrating unit takes profit of the solar altitude tracking, which the shading blinds already have, to increase system performance. A dynamic energy simulation has been conducted in two different locations—Sde Boker (Israel) and Avignon (France)—both with adequate annual irradiances for solar applications, but with different weather and energy demand characteristics. The simulation engine utilized has been TRNSYS, coupled with MATLAB (where the ray-tracing algorithm to simulate the holographic optical performance has been implemented). The concentrator achieves annual mean optical efficiencies of 30.3% for Sde Boker and 43.0% for the case of Avignon. Regarding the energy production, in both locations the thermal energy produced meets almost 100% of the domestic hot water demand as this has been considered a priority in the system control. On the other hand, the space heating demands are covered by a percentage ranging from 15% (Avignon) to 20% (Sde Boker). Finally, the electricity produced in both places covers 7.4% of the electrical demand profile for Sde Boker and 9.1% for Avignon.

Keywords: solar energy; solar concentration; photovoltaics; PVT; holographic optical elements (HOE); building integration; energy dynamic simulation

1. Introduction

Energy consumption in the building sector represents 40% of the total energy consumed in the European Union. The European Commission, in order to decrease energy consumption, defined (considering buildings as a priority) the directive which states the "20-20-20" objectives: greenhouse gas emissions reductions (20%), the share of renewable energy (20%) and improvements in energy efficiency (20%) [1]. In this regard, building integrated solar hybrid Concentrating Photovoltaic-Thermal (CPVT) systems are a technology which perfectly addresses the objectives defined by the European Union, as may cover both the thermal and the electrical consumption needs.

CPV systems replace part of the cell area by cheaper and more environmentally friendly materials, the optical elements, which can lead to more cost-efficient systems from both, economic and environmental aspects [2]. On the contrary, when increasing the concentration ratio the percentage which is not converted into electricity becomes much higher in absolute terms. This could cause PV overheating and thus, problems related with efficiency reduction, stress of materials, etc. arise.

A strategy to profit the removal heat which negatively influences system performance is to use a hybrid Photovoltaic-Thermal (PVT) receptor. A PVT module controls PV temperature while simultaneously produces thermal energy. Another strategy to prevent the PV warming up is the spectral selection of the incident irradiance. A technology able to concentrate sunlight and at the same time to spectrally select irradiance is holography.

Among the different types of Holographic Optical Elements (HOEs), volume holograms have been studied as solar concentrators attending to some interesting properties as the high optical efficiency achieved (they can reach 100% efficiency for a selected wavelength). They may be utilized in different configurations [3]: plane gratings, that are not concentrating elements but as they operate directing light toward the same area the incident irradiance is concentrated [4–6] or concentrating optical elements (lenses) either cylindrical [7,8] or spherical [9–11].

HOEs present two main characteristics that affect their performance: angular and chromatic selectivity, in other words, their efficiency depends on the angle of incidence and the wavelength. Consequently, the solar spectrum and the spectral sensitivity range of the photovoltaic cell, among other parameters, need to be taken into account in the design of the HOE, in order to optimize its behavior for the wavelength range of interest. The chromatic selectivity of holograms provides an important advantage in comparison with refractive elements, since the concentration of undesired wavelengths on the photovoltaic cell is avoided. If the HOE is designed to diffract infrared wavelengths with very poor efficiency, the cell is prevented from overheating, which could cause a worsening on the cell's performance [12,13]. The chromatic selectivity also allows spectrum splitting, if a configuration with more than one kind of receiver (either different photovoltaic cells [8,9] or a hybrid photovoltaic-thermal receiver [10,14–16]) is chosen.

More specifically, regarding holographic PVT designs: Vorndran et al. [10] proposed a spectrum-splitting holographic system in which a holographic lens diffracts a narrow bandwidth towards a photovoltaic cell. The transmitted spectrum is reflected on a parabolic mirror towards a thermal tube. The solar concentrator described by Froehlich et al. [15] is formed by two stacked holographic lenses, each composed by a holographic grating to correct the incident direction and a holographic lens. Each holographic lens directs a different spectral range of the incoming light to a photovoltaic cell, sensitive to one of these two spectral bandwidths. The transmitted spectrum reaches a thermal absorber, which also refrigerates the PVs. Xia et al. [16] proposed a solar concentrator formed by a holographic grating, which would split the incident spectrum into visible and infrared range, and a Fresnel lens, which would concentrate the visible spectrum onto a set of PV cells and the IR spectrum onto a heat exchanger. Iurevych et al. [14] simulated the performance of a solar concentrator constituted by a reflection holographic grating. Incoming rays with wavelengths of a certain range are reflected by the HOE and the surfaces of the system, reaching a PV cell, whereas the rest are transmitted through the HOE and reach a thermal absorber.

Based on the previous studies found in the literature, it can be noted that even though there are some works conducting optical and energetic simulation of holographic concentrators, there is no research dealing with the energy simulation of the system performance considering more than the concentrating unit itself. In this regard, the present research aims at covering an important gap in the frame of Holographic Concentrating Photovoltaic-Thermal (HCPVT) solar generators, which is their dynamic energy simulation. For this purpose, a two-floor family house with an occupancy of three people is simulated for two different locations: Sde Boker (Israel) and Avignon (France), analyzing the thermal and electrical production under both climatic conditions and energy demand profiles.

2. System Description

The analyzed building integrated concentrating PVT system is designed to be superimposed on the blinds of a solar louvre shading system. In this manner, the concentrator is benefitted from the solar altitude tracking of the shading blinds and thus increasing the optical efficiency. Figure 1 illustrates the architectural configuration proposed, indicating in light blue the blind area where the

concentrating system is placed (top-left). The blinds' size is 9 m long by 0.4 m wide and by 0.065 m high. The simulated building is considered to be 5.8 m height, starting the blinds at the ground floor window level (1 m height), therefore the number of blinds is 12. On the top-right, a schematic of a blind section shows the location of the holographic lenses and the PVT module, which is placed in the interior space. Both elements are assembled in a single unit forming a modular system with two parallel layers, the HOEs and the PVT module. At the bottom, a diagram of the cross section indicates the main dimensions of the module.

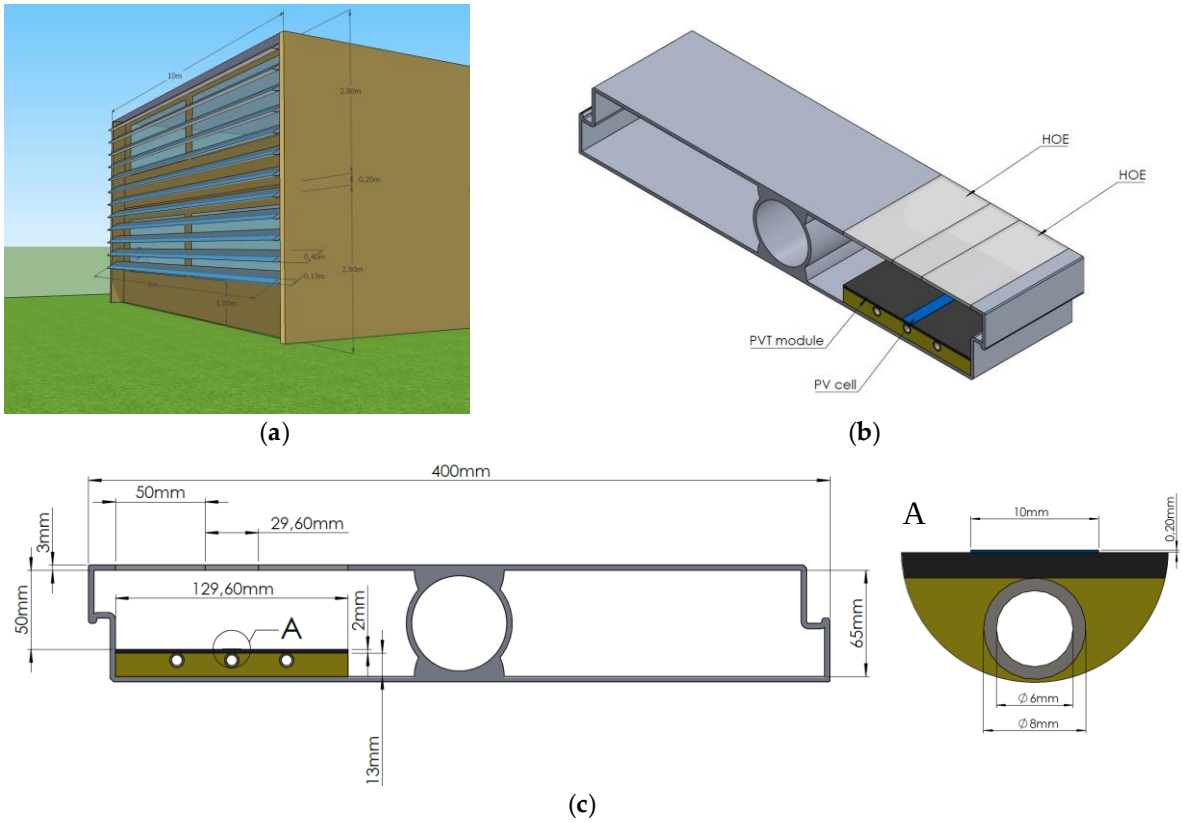

Figure 1. Architectural image of the building integrated concentrator (**a**), section of the blind where the PVT concentrator in placed (**b**) and cross-section and detail of the blind with the PVT concentrator (**c**).

The concentrating system consists of two holographic lenses that focus incident irradiance toward the PVT module. Both lenses are attached to the same glass substrate, which at the same time closes the space between them.

A diagram of the ray-tracing is represented in Figure 2. Three different wavelengths in the range of maximum spectral response of the Si PV cell are depicted to show the rays' spatial distribution at the *YZ* plane. On the right, a sketch illustrating the rays in the direction of the blind longitude represents the incidence along the x-axis (*XZ* plane), which corresponds to the solar azimuth movement. In this dimension, the length of the PVT receiver is slightly shorter than the length of the holographic lens to avoid vignetting effects. The azimuth angle translated to the entrance pupil's plane is named as φ. The maximum φ accepted by the concentrator is indicated in the figure.

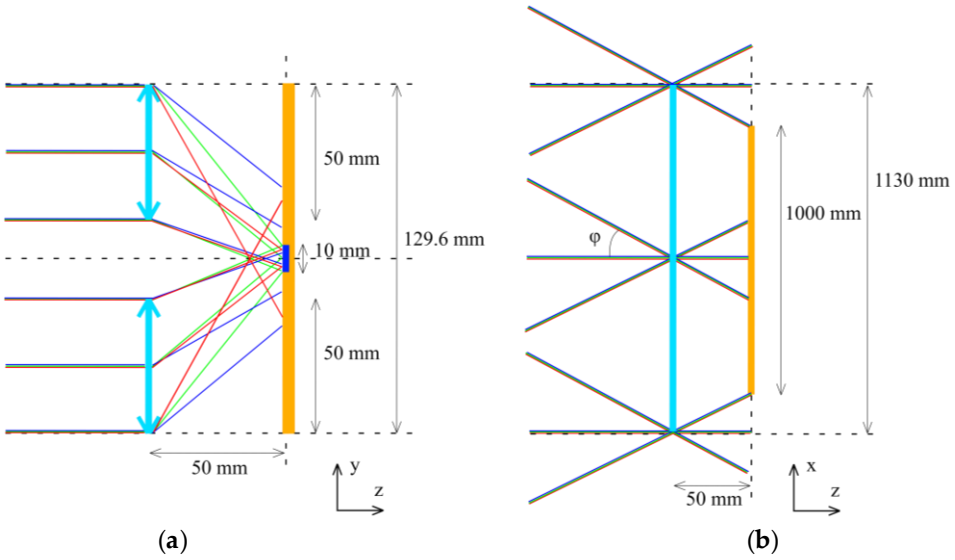

Figure 2. Schematic of the HCPVT generation unit, with ray-tracing for rays with three different wavelengths: 700 (depicted with blue lines), 800 (green lines) and 900 nm (red lines), at the *YZ*- (**a**) and *XZ*-plane (**b**).

2.1. Holographic Optical Element

A cylindrical holographic lens is chosen as a solar concentrator HOE. The recording of such lens is carried out by means of the interference of a plane wave and a cylindrical wave onto a photosensitive medium, as shown in Figure 3. This turns into variations of the refraction index along the material.

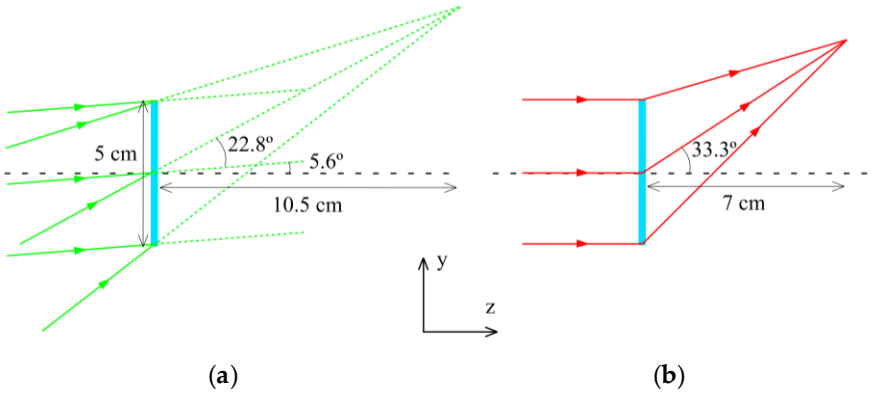

Figure 3. Sketch of the recording (**a**) at 532 nm, and reconstruction (**b**) at 800 nm schemes of the holographic cylindrical lens simulated in this study.

When illuminating a volume hologram at the reconstruction stage, only two waves are found at its output: the transmitted wave and the diffracted wave. With the adequate incident conditions (wavelength and angle), the efficiency of the diffracted beam is maximal, and it can reach 100% for a selected wavelength if the design is also optimum. When illuminating a holographic cylindrical lens with a plane wave, the resulting diffracted wave is a cylindrical one, as it is shown in Figure 3.

The reconstruction wavelength for which the HOE will be most efficient is set at 800 nm. This value results from a compromise between the incident solar spectrum (with maximal intensity at wavelengths around 500–800 nm most of the day) and the photovoltaic cell sensitivity (optimum around 700–1000 nm for mono-Si cells). Incident light at 800 nm will focus at a line parallel to the *x*-axis, 7 cm away from the HOE, as it is shown in Figure 3. However, the PVT module is placed at 5 cm away from

the HOE, in order to collect more energy of the desired wavelength range, since rays with different wavelengths are led towards different directions, as it is illustrated in Figure 2.

Holograms present higher angular selectivity when the incidence direction varies in the plane formed by the two recording beams, and lower in the perpendicular plane. Taking advantage of this effect, a cylindrical lens offers the possibility of suppressing tracking in one direction. Therefore, tracking is only necessary along the direction with higher angular selectivity.

The proposed recording material of the HOE is Bayfol HX, a photopolymer manufactured by Covestro AG (formerly Bayer MaterialScience) [17], adequate for holographic recording with solar photovoltaic applications [18].

In the configuration chosen for this study, two HOEs are placed separated in the same *XY*-plane, so that the spatial distributions of the diffracted beams are symmetrical. A glass plate located in this plane serves as a substrate for the photopolymer, covers the space between the two HOEs and is assumed to have the same refractive index as the photopolymer. The distance between the two lenses, and therefore, the position of the PV cell in the *y*-axis, was optimized so that it would receive more energy at the most favourable wavelength range for the cell. The ratio between the x dimension of the HOEs and the PV cell was chosen to avoid vignetting on the cell of its optimal wavelength range (700–1000 nm). Angles of incidence φ larger than the one depicted in Figure 2, when vignetting would occur for the optimal bandwidth, result in total internal reflection and prevent the former effect.

2.2. Hybrid Photovoltaic-Thermal Module

The PVT module units are considered to be 100 cm long by 12.96 cm wide; thus every shading blind of 9 m is composed of nine PVT modules. Every PVT module is formed by seven 14.29 cm long by 1 cm wide cells connected in series. The photovoltaic cells considered in the simulation are based on commercial mono-crystalline cells by Sunways [19], whose main electrical characteristics are summed up in Table 1. The characteristics of the thermal receiver are detailed in Section 3.2.

Table 1. Parameters of the PV cells, reprinted with permission from [19], copyright Sunways AG · Photovoltaic Technology · Max-Stromeyer-Str. 160 · D-78467 Konstanz. SD310912A version 03/13 EN.

V_{OC} (V)	J_{SC} (A/m^2)	*FF* (%)	γ (%/°C)	T_{NOCT} (°C)
0.635	377.6	78.4	−0.44	45

Notes: V_{OC} = Open circuit potential; J_{SC} = Short circuit current density; *FF* = Fill factor; γ = Power temperature dependence losses; T_{NOCT} = Nominal operating cell temperature.

3. Methodology

3.1. Spectra Simulation

The direct normal irradiance spectrum is calculated with the SMARTS radiative model [20], whose main atmospheric input parameters are (listed by order of importance): Air mass (*AM*), aerosol optical depth (τ), precipitable water (*PW*) and Ångström exponent (α).

Air mass is the parameter that normally affects more the spectrum. It is defined as the relative distance to the shortest vertical path length the sunrays traverse through the atmosphere before impacting the Earth's surface. SMARTS calculates the *AM* from the solar zenith angle (Z) for the location and time considered:

$$AM = \left[\cos Z + 0.45665 Z^{0.07} \left(96.4836 - Z\right)^{-1.7960}\right]^{-1} \quad (1)$$

τ refers to the quantity of aerosols in the vertical direction (urban haze, smoke particles, desert dust, sea salt ...) and characterizes its radiative strength. The τ at wavelength (λ) is linked to the Ångström exponent (α) by the Ångström law, where β (also called Ångström turbidity coefficient) is the aerosol optical depth at $\lambda = 1$ µm.

$$\tau = \beta\lambda^{-\alpha} \quad (2)$$

Values of α greater than 2 indicate the presence of fine particles (e.g., smoke particles or sulphates), whereas values close to zero are typically related to the presence of coarse particles, such as sea salt or desert dust [21].

Finally, *PW* is the total amount of condensed water (expressed in cm) corresponding to the total water vapour contained in a vertical atmospheric column above any location. Water vapour has strong absorption bands in the near infrared, which directly impacts the spectrum.

Measured values of *Z*, τ, *PW* and α, can be obtained from the Aerosol Robotic Network (AERONET) database [22]. For this study, only AERONET's level 2.0 data are used to guarantee the highest possible data quality (after cloud screening, calibration and degradation correction [23]).

τ at 500 nm and α (obtained between 440 and 870 nm) are retrieved. The latter provides both the α1 and α2 values required by SMARTS. This approach is considered because the single-α model is closer to the original Ångström definition and experimental errors associated with small-band determinations of the τ variation are decreased [24].

Detailed information on the sunlight spectrum for at least a complete year is required in order to accurately estimate the energy output of the PVT module. Therefore, a preliminary search on AERONET's database has been done to select only those locations and years with a high density of atmospheric retrievals. These retrievals are performed at least every 15 min for *AM* less than 5. Following the procedure described by Chan et al. [25], measurement gaps longer than 15 min are considered to be caused by extended cloudiness, not computing this time for the annual yield. In addition, the selected locations should be suitable for CPVT systems and have a high direct normal irradiance (DNI).

Two different locations have been selected according to three criteria: (i) they should be representative of different climatic conditions to provide not only differential spectral conditions, but also different electrical and thermal energy demands; (ii) they should provide high-quality data over an extended period of time (a constraint satisfied by only a small fraction of AERONET sites); and (iii) they should have co-located and simultaneous DNI measurements, in order to validate the simulated spectra. Based on the above criteria, Sde Boker, Israel, (2004) and Avignon, France, (2003) have been chosen (Table 2).

Table 2. Characteristic parameters for the selected locations.

Location	Simulated Year	Lat. (°)	Long. (°)	Elevation (m)	Mean Daily DNI (kWh/m^2/day) [26]	Annual Mean Atmospheric Parameters *AM* | τ | *PW* | α
Sde Boker	2004	30.86	34.78	480	6–6.5	1.92 | 0.18 | 1.34 |0.86
Avignon	2003	43.93	4.88	32	5–5.5	2.16 | 0.25 |1.76 | 1.37

Figure 4 illustrates the monthly variation of the most representative atmospheric parameters obtained by AERONET at the selected locations. These graphs conveniently display the amplitude with which each variable varies throughout the simulation year.

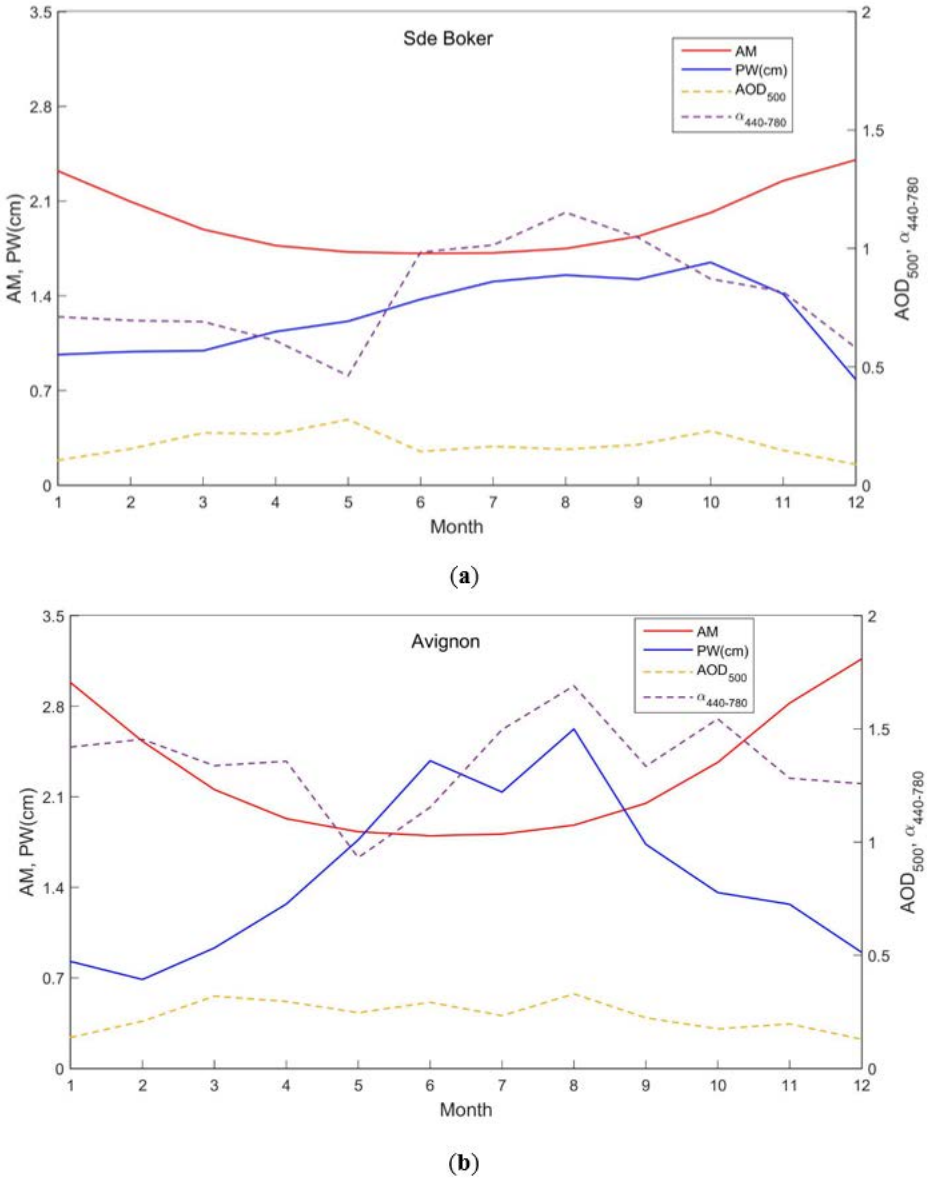

Figure 4. Monthly-average values of the main atmospheric variables for the simulated sites, obtained from AERONET. In the case of *AM*, the values are limited to $AM < 5$, in agreement with AERONET measurements. (**a**) Sde Boker and (**b**) Avignon.

Finally, the validation of the spectra generated by SMARTS is undertaken by comparing the calculated broadband DNI to reference irradiance measurements obtained from the Baseline Surface Radiation Network (BSRN) [27]. A good agreement is achieved between the simulated and the measured data, as depicted in Figure 5, showing the irradiance profiles for two different typical days in both locations. It should be stressed that the large drops in the measured data, due to clouds obscuring the sun, are not modelled in the simulations. In the case of Avignon, the validation has been conducted using DNI data from the BSRN station in Carpentras, located around 28 km away.

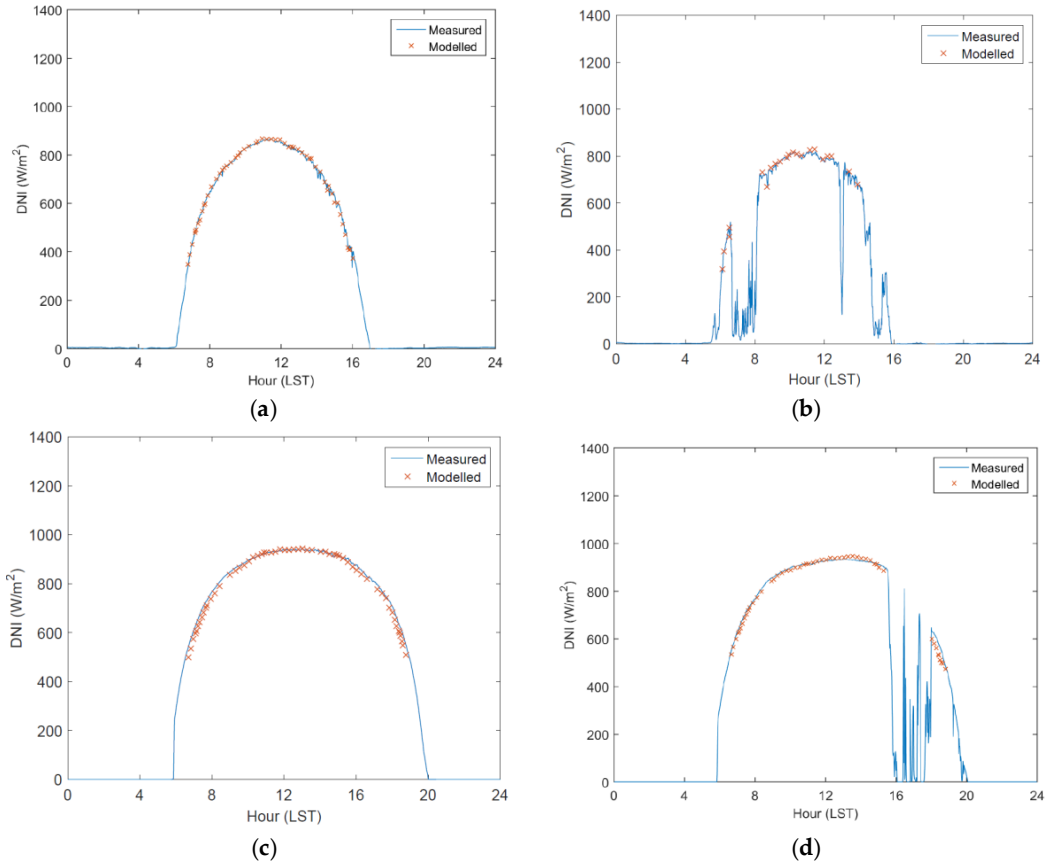

Figure 5. DNI data in Sde Boker under stable (**a**) and variable irradiance conditions (**b**) and in Avignon (**c**,**d**). The dates are respectively 19th of October, 20th of April, 1st of August and 30th of July in the selected simulated years. LST: Local standard time.

3.2. Optical Simulation

The performance analysis of the holographic lens is based on Kogelnik's Coupled Wave Theory [28] and the approximate scalar theory established by Syms [29]. A ray-tracing algorithm has been developed [30], which allows the calculation of the output directional cosines and the spectral energy associated with each ray, for the transmitted and the diffracted wave delivered to the PVT module.

The propagation wave vectors of the recording beams, $\vec{k}_1$ and $\vec{k}_2$, with modulus $k_1 = k_2 = 2\pi/\lambda_R$ (where λ_R is the recording wavelength), determine the grating vector $\vec{K} = \vec{k}_1 \pm \vec{k}_2$, illustrated in Figure 6.

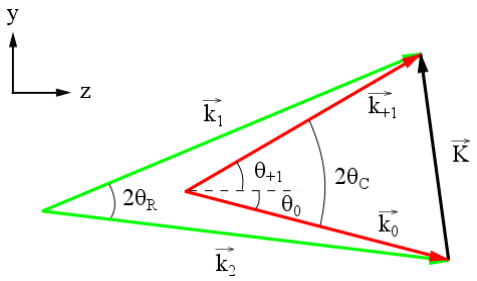

Figure 6. Sketch of the relation between the grating vector $\vec{K}$ and the wave vectors of the two recording beams, $\vec{k}_1$ and $\vec{k}_2$, and the transmitted and diffracted waves, $\vec{k}_0$ and $\vec{k}_{+1}$.

Since one of the recording beams is a cylindrical wave, its propagation wave vector has a different direction at each point along the y-direction, and the angle between beams is also different. Therefore, the vector $\vec{K}$, which is perpendicular to the planes with constant refractive index variation, is spatially dependant. Its modulus is $2\pi/\Lambda$, where Λ is the spatial period of a grating with vector $\vec{K}$, and also different at each point. Each point of the holographic lens behaves differently; thus, each point is treated as a local holographic grating.

When illuminating the HOE with a wave with vector $\vec{k}_0$ and a certain wavelength λ_C, the resulting diffracted wave has a vector $\vec{k}_{+1}$, which has the same modulus as $\vec{k}_0$ and direction determined with $\vec{k}_0$ and $\vec{K}$. This relation is shown in Figure 6. Thus, if the vector $\vec{K}$ along the hologram is known, the direction of the diffracted ray originated with each incident reconstruction ray at a certain point can be calculated.

The energy of the diffracted wave from each point is calculated with Equation (3):

$$\eta = \frac{\sin^2\left[\left(\nu^2 + \xi^2\right)^{1/2}\right]}{1 + \frac{\xi^2}{\nu^2}} \tag{3}$$

The parameters ν and ξ are given by:

$$\nu = \frac{\pi d \Delta n}{\lambda_C c_0 c_{+1}} \tag{4}$$

$$\xi = \frac{d\vartheta}{2c_{+1}} \tag{5}$$

where d is the thickness of the recording material, Δn is the refraction index modulation, λ_C is the reconstruction wavelength, and c_0 and c_{+1} are the directional cosines with respect to the z-axis of the reconstruction and diffracted wave, respectively. ϑ is a parameter that determines the variation from Bragg's law, that is, the condition of maximal efficiency. Bragg's law is met when the next equation is fulfilled:

$$2\Lambda \sin\theta_C = \lambda_C \tag{6}$$

where θ_c is the semiangle between the transmitted and the diffracted beam, shown in Figure 6. When Bragg's condition is not fulfilled the efficiency of the diffracted wave decreases, and the efficiency of the transmitted wave increases.

The energy of the transmitted wave is calculated as the remaining available energy that is not taken by the diffracted wave, at each point and for each reconstruction wavelength. The rays entering the system through the glass plate between the two HOEs are also considered.

The simulation considers the direct normal irradiance solar spectrum, generated by SMARTS, as the incident irradiance input parameter. Nevertheless, due to the implicit difficulty and computational time required, the solar semiangle and the diffuse irradiance fraction are not considered at this stage. Further research will be conducted to define the algorithm containing the particular angles of incidence and polarization constraints of the diffuse radiation, jointly with the implementation of the solar semiangle. Therefore, it should be taken into account that the irradiance delivered by the holographic concentrator is underestimated in a percentage proportional to the diffuse fraction at each simulated location. Losses due to Fresnel reflections on the surface and to total internal reflection [31] are taken into account in the simulations.

3.3. Energetic Simulation

The energetic simulation is conducted in TRNSYS, evaluating the HCPVT performance under the weather and energy demand conditions of Sde Boker and Avignon. Figure 7 charts the monthly

cumulated DNI values and the monthly average ambient temperatures in both locations. In Sde Boker the annual cumulated DNI is 2445 kWh/m^2 and the annual mean temperature is 18.3 °C, in Avignon these values are 1860 kWh/m^2 and 14.7 °C respectively. It should be noticed that, in agreement with AERONET criteria, values with $AM > 5$ (solar altitude below 11.5°) are not considered and, taking into consideration the optical efficiency limitations of the concentrating system, the direct beam irradiances accepted by the HCPVT module will be significantly lower than the DNI values. Results regarding optical efficiencies are included in Section 4.

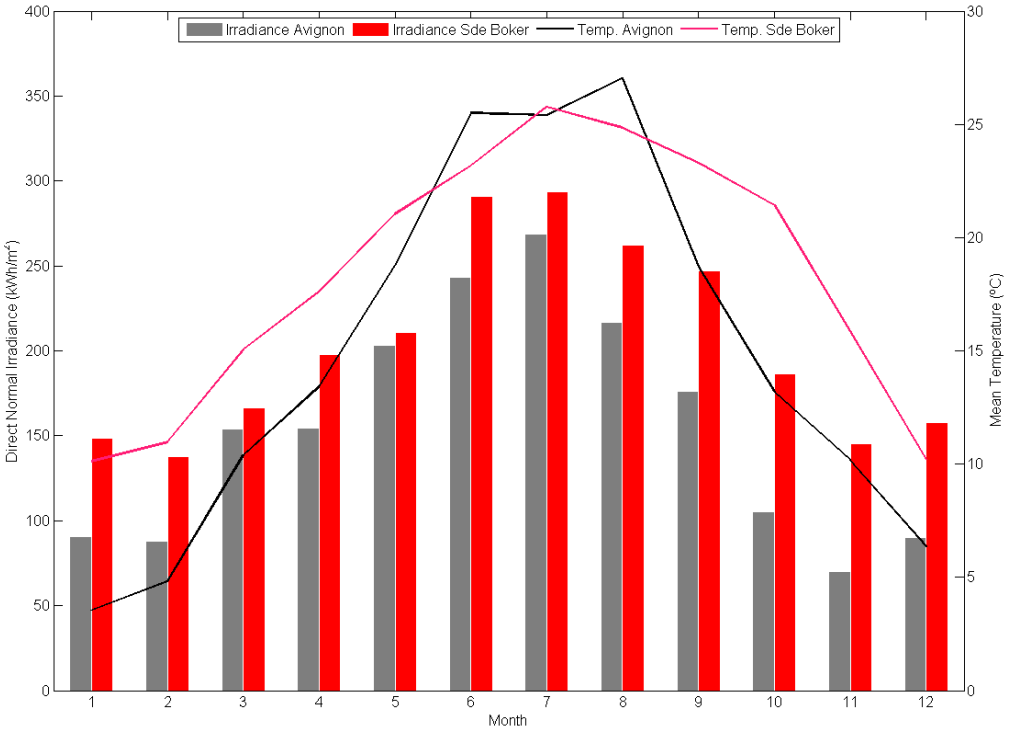

Figure 7. Monthly cumulated DNI and mean temperature values.

The energy demand considered corresponds to a three person individual family house with two floors of 80 m^2 each. The main façade, where the solar system is installed, is south-oriented. The thermal demand for space heating (SH) has been determined using the TRNBUILD tool considering the following thermal transmittance coefficients: 0.74 W/m$^2\cdot$°C for the exterior walls, 0.5 W/m$^2\cdot$°C for the roof and 2.1 W/m$^2\cdot$°C for the windows. The space heating load is calculated to maintain the interior temperature at 20 °C. The domestic hot water (DHW) demand has been determined assuming a water consumption of 30 liters per person at 60 °C.

The electrical energy demand profiles have been estimated to reflect the importance of the air conditioning consumption during hot months, representing the highest load in Sde Boker, and a profile where the minimum of the curve is centered in summer (Avignon).

The cumulated annual energy demands for DHW, SH and electricity at Sde Boker and Avignon are listed in Table 3. As it can be appreciated, the DHW energy demand is 23% higher at Avignon than at Sde Boker due to its lower ambient temperatures. The same behavior is observed in the SH demand, whose value at Avignon is more than twice the one at Sde Boker, considering the colder climate during winter period. Conversely, in the case of the electrical energy demand the annual value at Sde Boker is quite bigger than at Avignon (24%) because of the air conditioning load during the hot months.

Table 3. Energy demand cumulated annual values.

Location	DHW (kWh)	SH (kWh)	Electricity (kWh)
Sde Boker	1589	7813	4433
Avignon	1955	16624	3575

Once determined the energy demands for both places, the following system topology has been implemented in the simulation for both locations (Figure 8):

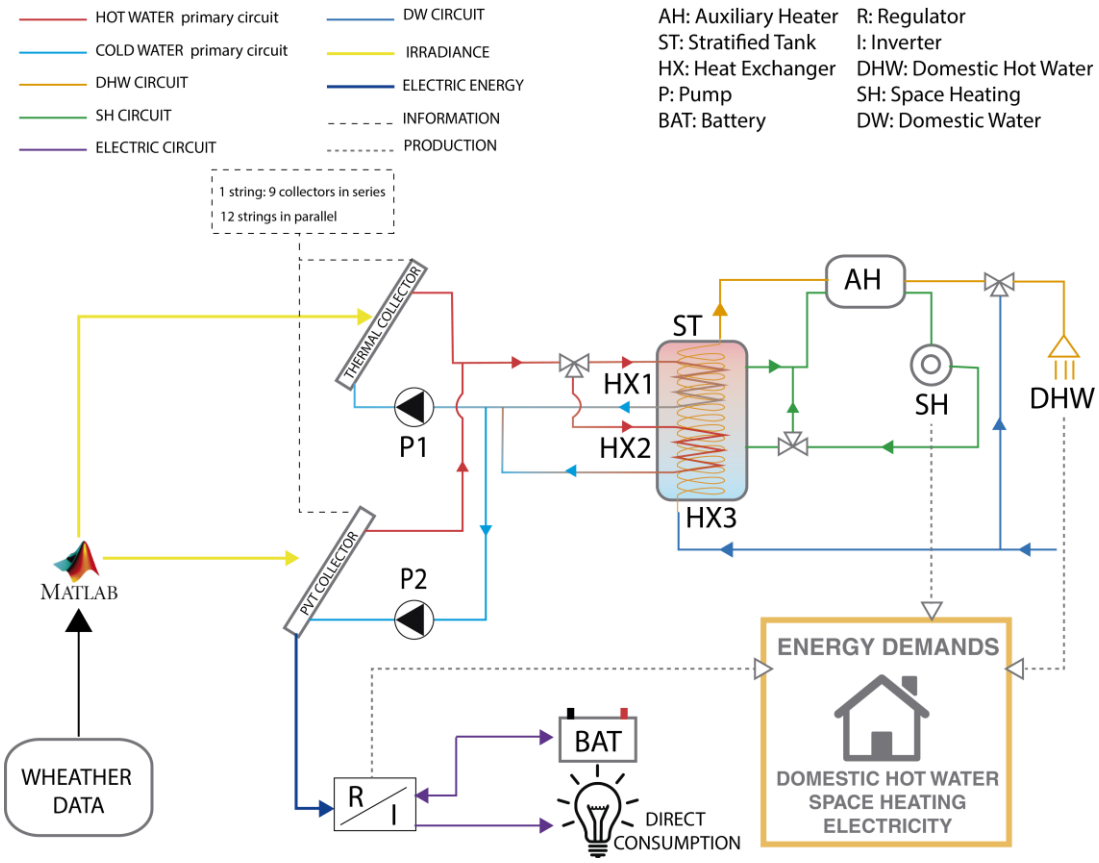

Figure 8. Simulated system topology.

The optical simulation program described in Section 3.2, which is programmed in MATLAB, is linked to TRNSYS delivering at every time step (1 min) the irradiance impacting on the PVT module, differentiating between the PV cell area where the irradiance is concentrated, named PVT collector, and the rest of the module, which is indicated in the system topology scheme as thermal collector (see Figure 8). From the irradiance received on the module, the thermal energy produced is calculated in two different ways: (i) for the receiver where there is no PV cell a standard *type 1b* has been used including the characteristics of a real commercial thermal module specified in Table 4; (ii) for the receiver where the PV is situated, strictly the PVT, a MATLAB code has been programmed which determines the electrical power (P'_{mpp}) coupled with the thermal generator *type 1b*, as a function of the solar cell electrical parameters and the cell temperature, calculated with the following Equation (7) [32]:

$$P'_{mpp} = P_{mpp}\left[1 + \gamma\left(T_{cell} - 25\right)\right] \quad (7)$$

where P_{mpp} is the electrical power generated by a PV cell without taking into account losses due to the temperature, γ is a temperature coefficient equal to $-0.44\%/^{\circ}C$ for the PV cells considered in this

study, and T_{cell} is the temperature of the cell in °C. The temperature of the cell of the PVT module is estimated with Equation (8) [33]:

$$T_{cell} = T_{in} + \frac{P_{th}}{F' U_L A} \left(1 - F'\right) \tag{8}$$

where T_{in} is the input temperature of the water circulating at each module, P_{th} is the power generated by the thermal absorber, F' is the collector efficiency factor, U_L is the overall convective heat loss coefficient of the collector and A is the surface of the collector. T_{in} and P_{th} values are obtained from the previous time step, considering the error to be minimum.

Table 4. Parameters of the thermal collector [34].

η_0 (%)	U_L (W/m^{2}K)	k_2 (W/m^{2}K^2)	F'	ε (%)	α (%)	τ (%)
79.9	3.97	0.016	0.913	5.0	95.5	91.6

η_0 = Efficiency; U_L, k_2 = Coefficients of heat loss; ε = Emission; α = Absorption; τ = Transmission and F' = Collector efficiency factor ($F' = \eta_0/\tau\alpha$).

The electrical power of the cell P_{mpp} without temperature effects is calculated with:

$$P_{mpp} = J_{SC} V_{OC} FF \tag{9}$$

The short circuit current, J_{SC} is calculated taking into account the spectral response curve of the mono-crystalline silicon solar cell manufacturer. The values of the open circuit voltage V_{OC} and the fill factor FF are assigned from the technical characteristics of the simulated solar cells (see Table 1).

4. Results

The optical efficiency of the concentrating holographic system is defined in Equation (10) as the ratio between the irradiance received at the generator surface, differentiated in the area where the PV is situated (A_{PV}) and the rest of the area where it is the thermal absorber (A_T), and the irradiance at the entrance pupil area of the system (A_E). The irradiances on the PV, thermal absorber and entrance pupil are respectively I_{PV}, I_T and I_E:

$$\eta_{opt} = \frac{I_{PV} A_{PV} + I_T A_T}{I_E A_E} \tag{10}$$

The average optical efficiency obtained each month with the solar irradiance of both locations is presented in Figure 9. The fact that the system works better during the winter months than the summer months may seem counterintuitive. However, it is due to the lack of tracking of the system in the azimuth direction, since the maximum optical efficiency is reached when the azimuth angle, φ, is zero (at solar midday), and decreases when the absolute value of this angle increases.

The azimuth angle reaches greater values in summer; therefore, the optimum incident angle range is found during less time each day, which results in lower optical efficiency, because of the angular selectivity of the HOEs. It should also be noticed that the performance of the optical system is better for Avignon than for Sde Boker, since the latter is located at lower latitude, and has larger values of φ along the year than Avignon. Moreover, the building integration imposes geometrical restrictions on the system: although it tracks the solar altitude movement of the sun, too large values of this parameter (which occur at solar midday in the summer months at Sde Boker) cause shading between blinds, and then the incident irradiance does not impact on the concentrator for those time periods.

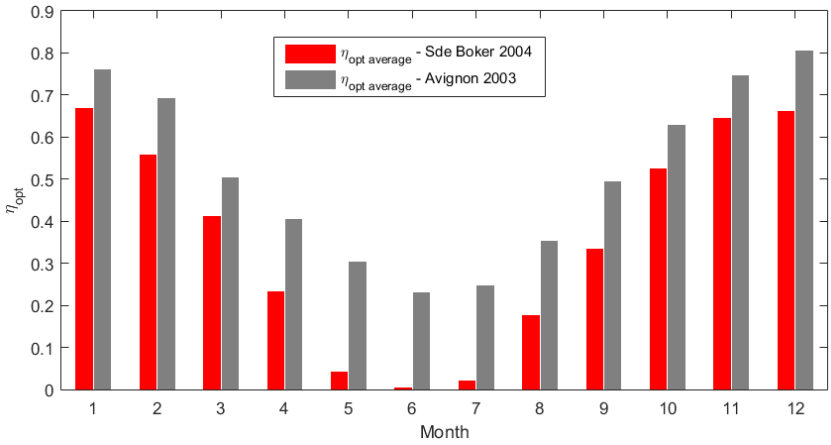

Figure 9. Average optical efficiency of the concentrating holographic system obtained each month with incident radiation of Sde Boker (2004) and Avignon (2003).

The incident mean annual spectral irradiance received at the surface of the PV cell and at the surface of the thermal absorber, determined by means of the optical simulation described in Section 3.2, is plotted in Figure 10, together with the incident solar spectral irradiance received at the entrance of the system. One of the most remarkable aspects of this graph is the shift of the peak wavelength of the spectrum that reaches the PV cell, compared to the solar spectrum. This effect is caused by the chromatic selectivity of the HOEs, which are designed to perform more efficiently around 800 nm. It is also clearly noticeable the difference between the spectra of Sde Boker and Avignon: due to the angular selectivity of the HOEs, the optical concentrator is more efficient at Avignon's latitude, although the incident irradiance is higher at Sde Boker. This results in a maximum incident irradiance value on the PV cell that doubles the maximum of the solar incident irradiance in Avignon. The shape of the spectral irradiance received by the thermal absorber is rather similar to the solar spectra of both locations, except for the optimum wavelength range of the PV cell. The irradiance received at Avignon is higher than the one received at Sde Boker, as expected.

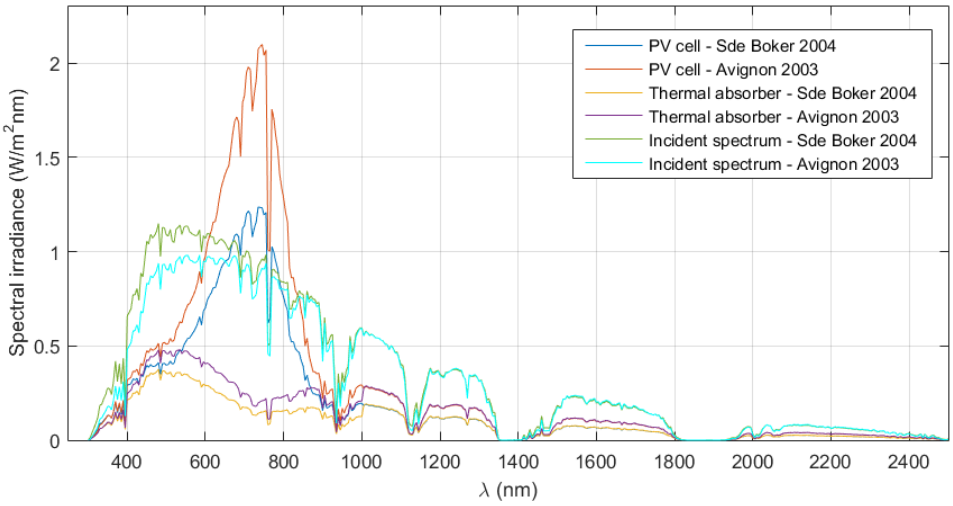

Figure 10. Average spectral irradiance at the entrance of the system, at the PV cell and at the thermal absorber at both locations.

The DHW energy demand is stated in the simulations to be satisfied prior to the SH demand. To evaluate the percentage of DHW demand that is covered by the HCPVT, the solar fraction is defined as:

$$SF_{DHW} = 100\left(1 - \frac{Consumption_{auxiliary,DHW}}{Demand\,DHW}\right) \quad (11)$$

In the case of Sde Boker, the solar thermal production covers well all the months except May, June and July. This happens because, as explained previously, the solar altitude is very high during these months and the system only accepts values lower than 71°. In the case of December, the values of production are not representative as only few days of atmospheric values are provided in AERONET. Following the tendency of the previous and next months a value of the solar fraction close to 100% should be expected (see Figure 11a). In Avignon, the HCPVT system accepts all the solar height angles, and in consequence the solar fraction takes a value of almost 100% in all the months. The annual solar production for DHW applications results in Sde Boker of 1218 kWh and in Avignon takes a value of 1869 kWh.

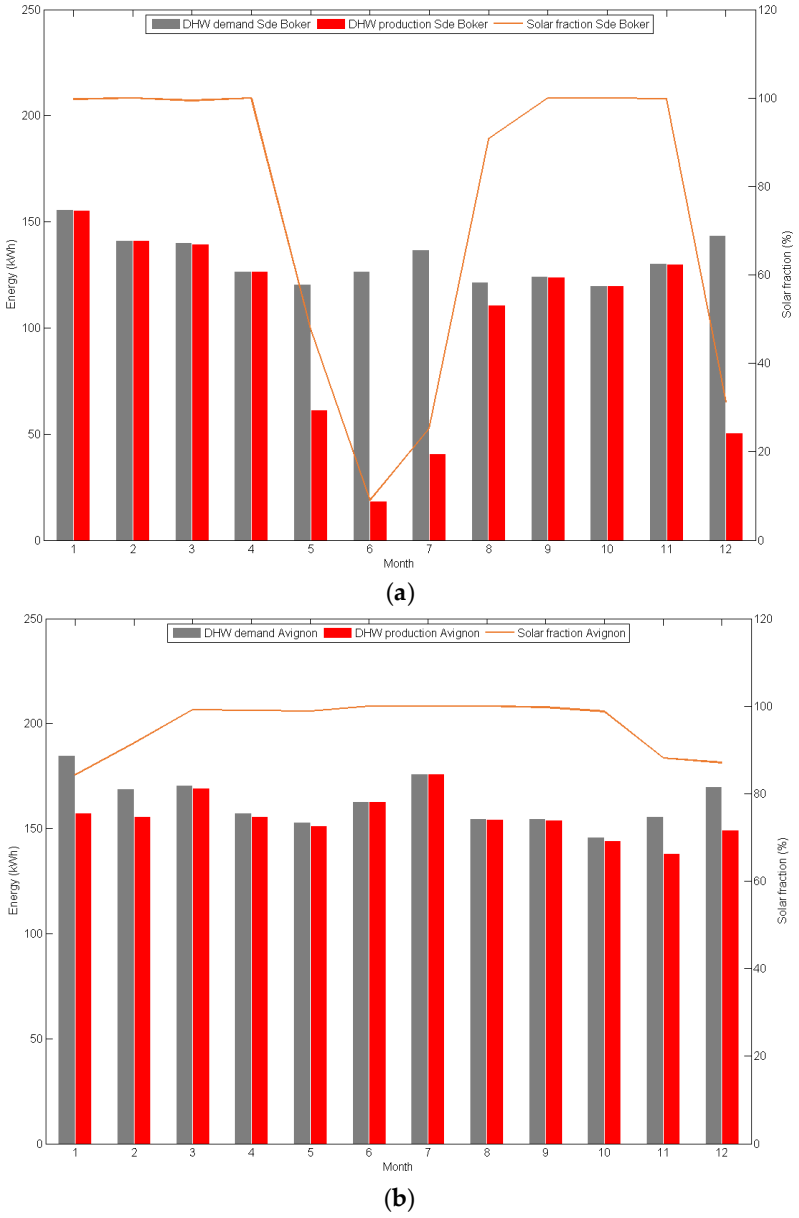

Figure 11. DHW energy demand, production and solar fraction in Sde Boker (**a**) and Avignon (**b**).

The solar production aims at partially covering the SH demand, taking into consideration that the collector total area is quite low, approximately 14 m^2. The heating system considered is a radiant floor which impulsion temperature is assumed to be 42 °C and the return one to be 34 °C. In an analogous manner than in the DHW, the solar fraction covering the SH demand is expressed as:

$$SF_{SH} = 100\left(1 - \frac{Consumption_{auxiliary,SH}}{Demand\,SH}\right) \quad (12)$$

Figure 12 plots the monthly SH demand and solar production, indicating that in Sde Boker there is no SH need during almost 6 complete months. In the rest of the months the solar fraction present values of around 20% (20.1%). On the contrary, Avignon is more demanding in SH energy, achieving in this case an average solar fraction of 15.8%.

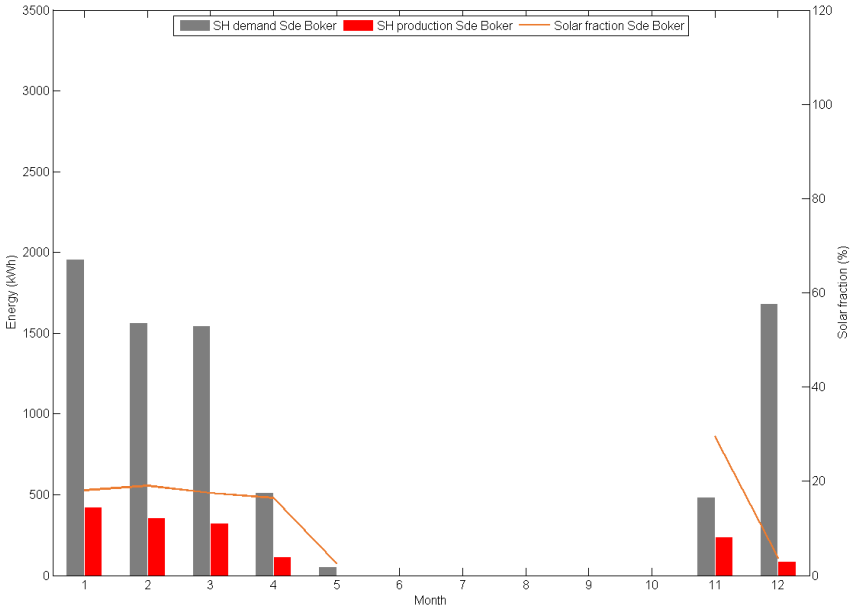

(**a**)

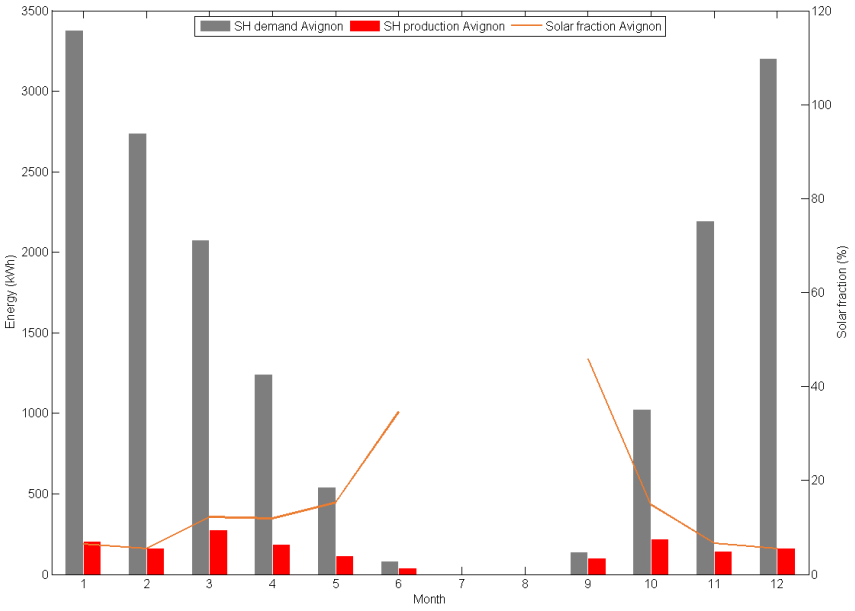

(**b**)

Figure 12. SH energy demand, production and solar fraction in Sde Boker (**a**) and Avignon (**b**).

The photovoltaic production results are included in Figure 13, where the solar fraction has been calculated with Equation (13). It can be seen that in both places the average solar fractions are near 10% (Sde Boker = 7.4% and Avignon = 9.1%), which is a very positive result considering that the PV net area is 1.08 m^2 and the electric demand values are important.

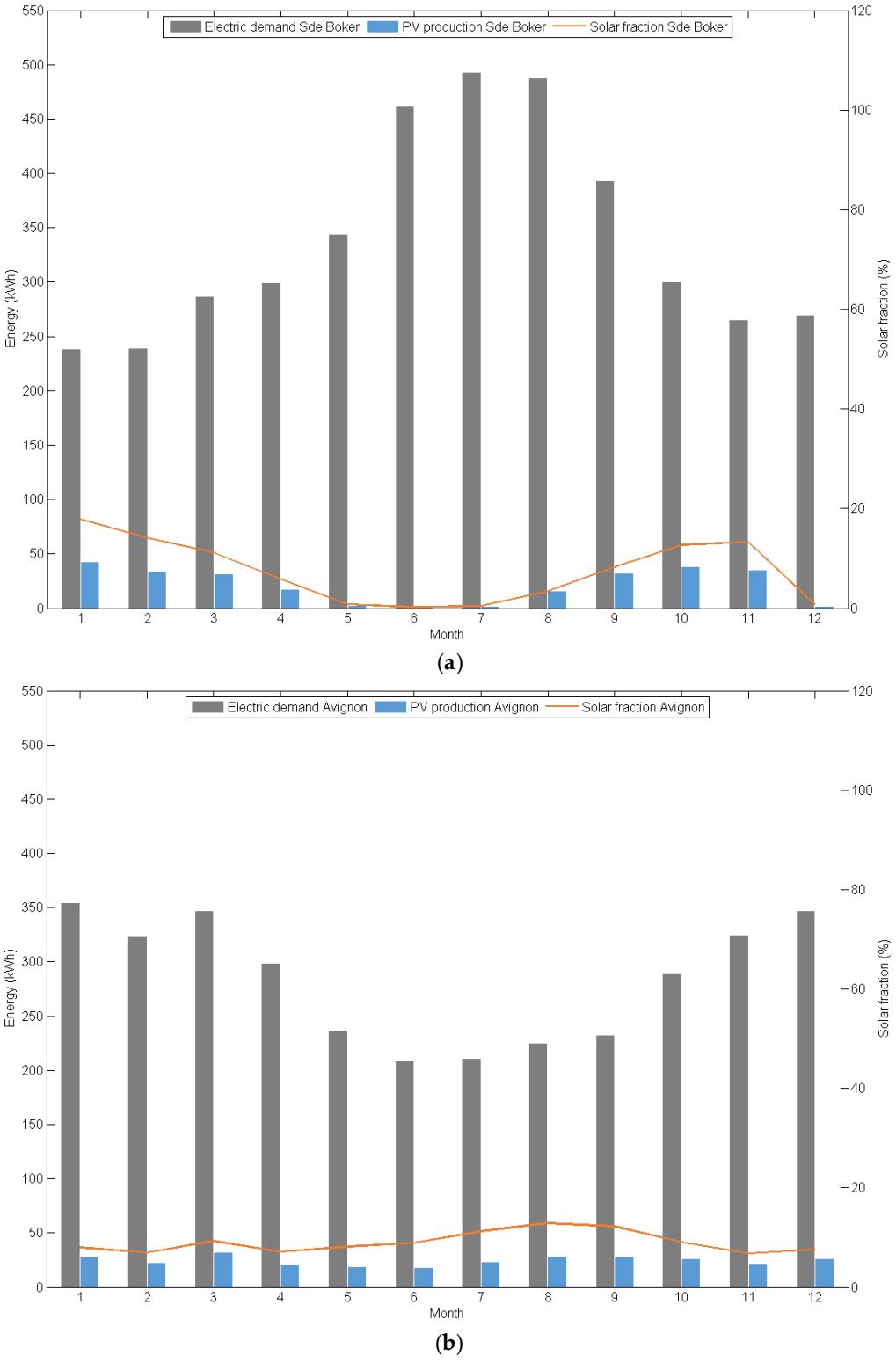

Figure 13. Electrical energy demand, production and solar fraction in Sde Boker (**a**) and Avignon (**b**).

This good performance is obtained due to the holographic optical element effect which concentrates on the cell only the bandwidth for which it is more sensitive and does not concentrated the infrared avoiding overheating. At the same time, the temperature of the cell is also controlled by the active cooling system incorporated in the PVT module (see Table 5):

$$SF_{PV} = 100 \left(\frac{Photovoltaic\ production}{Electric\ demand} \right) \quad (13)$$

Table 5. Summary of system efficiencies.

Month	Average Optical Efficiency (%)		Average Thermal Efficiency DHW (%)		Average Thermal Efficiency SH (%)		Average Electrical Efficiency (%)	
	Sde Boker	Avignon	Sde Boker	Avignon	Sde Boker	Avignon	Sde Boker	Avignon
January	67.1	76.3	11.9	19.7	28.2	22.0	22.4	16.6
February	56.1	69.5	12.5	21.7	27.7	19.2	27.7	15.2
March	41.4	50.5	13.1	16.8	26.6	23.9	23.5	17.0
April	23.3	40.6	17.2	20.3	14.2	20.9	29.9	14.3
May	4.3	30.4	45.8	23.0	1.0	15.0	22.6	15.8
June	0.7	23.1	56.3	27.2	0.0	5.7	23.1	16.8
July	2.2	24.8	51.5	23.4	0.0	0.0	24.4	16.8
August	17.8	35.5	18.9	17.0	0.0	0.0	19.7	16.8
September	33.5	49.6	11.4	17.2	0.0	9.9	23.7	16.5
October	52.6	63.1	10.0	16.2	0.0	21.2	21.9	14.7
November	64.7	74.9	11.6	23.1	18.5	20.1	19.7	16.9
December	66.2	80.6	17.5	22.0	28.9	20.5	17.6	17.3

Finally, in Table 5 the monthly average efficiencies of the main system components are presented. The optical efficiency values correspond to those plotted in Figure 9. It is important to highlight one of the most differential aspects of the present simulated system, which is the electrical efficiency values obtained. These values are high in comparison with standard PV installations, achieving in some months numbers above 25%. This performance is obtained, as mentioned previously, due to the proper combination of two factors: the active cooling and the spectrally selective concentration obtained by the HOEs.

5. Conclusions

A building-integrated holographic concentrating photovoltaic-thermal system has been designed and simulated. The module has been placed on the blinds of a solar louvre, which track the solar altitude movement of the sun along the day, on a south-oriented façade.

The direct normal irradiance solar spectra along one year have been calculated with the SMARTS radiative model, utilizing AERONET atmospheric parameters, for two locations (Sde Boker and Avignon), to test the concentrating system proposed under different conditions. These spectra have been verified with direct irradiance measurements obtained from the Baseline Surface Radiation Network (BSRN), which proved the high accuracy of the simulations.

The behavior of the holographic concentrator, based on two holographic cylindrical lenses, was simulated by means of a ray-tracing algorithm. It concentrates toward the cell mainly its optimal wavelength range and also distributes the rest of the spectral irradiance on the thermal absorber, reaching a total optical efficiency. The annual average optical efficiencies obtained for Sde Boker and for Avignon are 30.3% and 43.0%, respectively. A MATLAB-TRNSYS coupling was implemented to run simultaneously the optical, the thermal and the electrical simulation for the two locations weather data files.

The electrical energy generated by the PV cell aims at partially covering the electrical demand and the thermal energy produced by the module is managed to satisfy the domestic hot water energy (priority) and partially the space heating energy requirements, of a house of a three people family.

In the case of the domestic hot water energy demand, which was considered a priority, the average solar fractions found were 79.3% for Sde Boker and 95.5% for Avignon. On the other hand, the proposed system covered more than 15% of the space heating demand at both locations (Sde Boker = 20.1% and Avignon = 15.8%). Regarding the electrical energy produced, more stable values were obtained in the case of Avignon throughout the year; however, at both locations the mean annual values were quite satisfactory, near the 10% (Sde Boker = 7.4% and Avignon = 9.1%). A future work of the present study is the construction and experimental characterization for the system performance validation.

Acknowledgments: This research was supported by 'Ministerio de Economía y Competitividad' of Spain for the funding (grants ENE2013-48325-R and BES-2014-069596), the Generalitat de Catalunya (grant 2016 FI_B1 00019), the UdL-Santander Bank (UdL-Impuls grant) and the Diputación General de Aragón-Fondo Social Europeo (TOL research group, T76).

Author Contributions: The research team works in a collaborative manner and all the authors have contributed in all the sections of the present manuscript.

Conflicts of Interest: The authors declare no conflict of interest.

References

1. Directive 2010/31/EU of the European Parliament and of the Council of 19 May 2010 on the Energy Performance of Buildings. European Parliament: Strasbourg, France, 2010.
2. Menoufi, K.; Chemisana, D.; Rosell, J.I. Life Cycle Assessment of a Building Integrated Concentrated Photovoltaic scheme. *Appl. Energy* **2013**, *111*, 505–514. [CrossRef]
3. Collados, M.V.; Chemisana, D.; Atencia, J. Holographic solar energy systems: The role of optical elements. *Renew. Sustain. Energy Rev.* **2016**, *59*, 130–140. [CrossRef]
4. Zhang, D.; Castro, J.M.; Kostuk, R.K. One-axis tracking holographic planar concentrator systems. *J. Photonics Energy* **2011**, *1*. [CrossRef]
5. Castillo, J.E. Thermal effects of the extended holographic regions for holographic planar concentrator. *J. Photonics Energy* **2011**, *1*. [CrossRef]
6. Castro, J.M.; Zhang, D.; Myer, B.; Kostuk, R.K. Energy collection efficiency of holographic planar solar concentrators. *Appl. Opt.* **2010**, *49*. [CrossRef] [PubMed]
7. Chemisana, D.; Collados, M.V.; Quintanilla, M.; Atencia, J. Holographic lenses for building integrated concentrating photovoltaics. *Appl. Energy* **2013**, *110*, 227–235. [CrossRef]
8. Ludman, J.E.; Riccobono, J.; Semenova, I.V.; Reinhand, N.O.; Tai, W.; Li, X.; Syphers, G.; Rallis, E.; Sliker, G.; Martín, J. The optimization of a holographic system for solar power generation. *Sol. Energy* **1997**, *60*, 1–9. [CrossRef]
9. Zhang, D.; Gordon, M.; Russo, J.M.; Vorndran, S.; Kostuk, R.K. Spectrum-splitting photovoltaic system using transmission holographic lenses. *J. Photonics Energy* **2013**, *3*. [CrossRef]
10. Vorndran, S.; Russo, J.M.; Wu, Y.; Gordon, M.; Kostuk, R. Holographic diffraction-through-aperture spectrum splitting for increased hybrid solar energy conversion efficiency. *Int. J. Energy Res.* **2015**, *39*, 326–335. [CrossRef]
11. Ludman, J.E. Holographic solar concentrator. *Appl. Opt.* **1982**, *21*, 3057–3058. [CrossRef] [PubMed]
12. Xiao, C.; Yu, X.; Yang, D.; Que, D. Impact of solar irradiance intensity and temperature on the performance of compensated crystalline silicon solar cells. *Sol. Energy Mater. Sol. Cells* **2014**, *128*, 427–434. [CrossRef]
13. Chander, S.; Purohit, A.; Sharma, A.; Nehra, S.P.; Dhaka, M.S. A study on photovoltaic parameters of mono-crystalline silicon solar cell with cell temperature. *Energy Rep.* **2015**, *1*, 104–109. [CrossRef]
14. Iurevych, O.; Gubin, S.; Dudeck, M. Combined receiver of solar radiation with holographic planar concentrator. *IOP Conf. Ser. Mater. Sci. Eng.* **2012**, *29*. [CrossRef]
15. Froehlich, K.; Wagemann, E.U.; Frohn, B.; Schulat, J.; Stojanoff, C.G. Development and fabrication of a hybrid holographic solar concentrator for concurrent generation of electricity and thermal utilization. In Proceedings of SPIE, San Diego, CA, USA, 13–14 July 1993; pp. 311–319.

16. Xia, X.W.; Parfenov, A.V.; Aye, T.M.; Shih, M.-Y. Efficient hybrid electric and thermal energy generation. In Proceedings of SPIE, San Diego, CA, USA, 22–24 August 2011.
17. Berneth, H.; Bruder, F.-K.; Fäcke, T.; Jurbergs, D.; Hagen, R.; Hönel, D.; Rölle, T.; Walze, G. Bayfol HX photopolymer for full-color transmission volume Bragg gratings. SPIE Photonics West 2014-OPTO Optoelectron. *Devices Mater.* **2014**, *9006*. [CrossRef]
18. Marín-Sáez, J.; Atencia, J.; Chemisana, D.; Collados, M.-V. Characterization of volume holographic optical elements recorded in Bayfol HX photopolymer for solar photovoltaic applications. *Opt. Express* **2016**, *24*, A720. [CrossRef] [PubMed]
19. Sunways. Copyright: Sunways AG · Photovoltaic Technology · Max-Stromeyer-Str. 160 · D-78467 Konstanz. SD310912A version 03/13 EN. Available online: http://www.sunways.eu (accessed on 22 May 2013).
20. Gueymard, C.A. Parameterized transmittance model for direct beam and circumsolar spectral irradiance. *Sol. Energy* **2001**, *71*, 325–346. [CrossRef]
21. Eck, T.F.; Holben, B.N.; Reid, J.S.; Dubovik, O.; Smirnov, A.; O'Neill, N.T.; Slutsker, I.; Kinne, S. Wavelength dependence of the optical depth of biomass burning, urban, and desert dust aerosols. *J. Geophys. Res. Atmos.* **1999**, *104*, 31333–31349. [CrossRef]
22. Aerosol Robotic Network (AERONET). Available online: http://aeronet.gsfc.nasa.gov/ (accessed on 14 October 2015).
23. Holben, B.N.; Eck, T.F.; Slutsker, I.; Tanré, D.; Buis, J.P.; Setzer, A.; Vermote, E.; Reagan, J.A.; Kaufman, Y.J.; Nakajima, T.; et al. AERONET—A Federated Instrument Network and Data Archive for Aerosol Characterization. *Remote Sens. Environ.* **1998**, *66*, 1–16. [CrossRef]
24. Jaus, J.; Gueymard, C.A. Generalized spectral performance evaluation of multijunction solar cells using a multicore, parallelized version of SMARTS. In Proceedings of the AIP Conference, Toledo, Spain, 16–18 April 2012; Volume 1477, pp. 122–126.
25. Chan, N.L.A.; Brindley, H.E.; Ekins-Daukes, N.J. Impact of individual atmospheric parameters on CPV system power, energy yield and cost of energy. *Prog. Photovoltaics Res. Appl.* **2014**, *22*, 1080–1095. [CrossRef]
26. Solar and Wind Energy Resource Assessment (SWERA). Available online: https://maps.nrel.gov/swera (accessed on 27 May 2016).
27. World Radiation Monitoring Center—Baseline Surface Radiation Network Homepage. Available online: http://bsrn.awi.de/ (accessed on 27 May 2016).
28. Kogelnik, H. Coupled wave theory for thick hologram gratings. *Bell Syst. Tech. J.* **1969**, *48*, 2909–2947. [CrossRef]
29. Syms, R.R.A. Vector Effects in Holographic Optical Elements. *Opt. Acta Int. J. Opt.* **1985**, *32*, 1413–1425. [CrossRef]
30. Bañares-Palacios, P.; Álvarez-Álvarez, S.; Marín-Sáez, J.; Collados, M.-V.; Chemisana, D.; Atencia, J. Broadband behavior of transmission volume holographic optical elements for solar concentration. *Opt. Express* **2015**, *23*, A671–A681. [CrossRef] [PubMed]
31. Hecht, E. *Optics*; Addison Wesley: Reading, UK, 1998.
32. Marion, B. A method for modeling the current-voltage curve of a PV module for outdoor conditions. *Prog. Photovoltaics Res. Appl.* **2002**, *10*, 205–214. [CrossRef]
33. Amrizal, N.; Chemisana, D.; Rosell, J.I. Hybrid photovoltaic–thermal solar collectors dynamic modeling. *Appl. Energy* **2013**, *101*, 797–807. [CrossRef]
34. Schüco. Available online: https://www.schueco.com (accessed on 27 May 2016).